

Coma Volatile Composition and Thermal Physics in Comet C/2022 E3 (ZTF) Measured Near Closest Approach to Earth with NASA-IRTF

NATHAN X. ROTH,^{1,2,*} MICHAEL A. DiSANTI,^{3,*} BONCHO P. BONEV,^{2,*} NEIL DELLO RUSSO,^{4,*} ERIKA L. GIBB,^{5,*}
RONALD J. VERVACK, JR.,^{4,*} MOHAMMAD SAKI,^{5,*} ADAM J. MCKAY,⁶ HIDEYO KAWAKITA,⁷ STEFANIE N. MILAM,⁸
MARTIN A. CORDINER,^{8,9} AND K. D. FOSTER¹⁰

¹*Solar System Exploration Division, Astrochemistry Laboratory Code 691, NASA Goddard Space Flight Center, 8800 Greenbelt Rd., Greenbelt, MD 20771, USA*

²*Department of Physics, American University, 4400 Massachusetts Ave NW, Washington, DC 20016, USA*

³*Solar System Exploration Division, Planetary Systems Laboratory Code 693, NASA-Goddard Space Flight Center, 8800 Greenbelt Rd., Greenbelt, MD 20771, USA*

⁴*Johns Hopkins University Applied Physics Laboratory, 11100 Johns Hopkins Rd., Laurel, MD, 20723 USA*

⁵*Department of Mathematics, Physics, Astronomy, and Statistics, 1 University Blvd., University of Missouri-St.Louis, St. Louis, MO, 63121 USA*

⁶*Department of Physics & Astronomy, Appalachian State University, 525 Rivers Street, Boone, NC 28608 USA*

⁷*Koyama Astronomical Observatory, Kyoto Sangyo University, Motoyama, Kamigamo, Kita-ku, Kyoto, 603-8555, Japan*

⁸*Solar System Exploration Division, Astrochemistry Laboratory Code 691, NASA Goddard Space Flight Center, 8800 Greenbelt Rd., Greenbelt, MD 20771, USA*

⁹*Department of Physics, Catholic University of America, Washington DC, USA*

¹⁰*Department of Chemistry, University of Virginia, Charlottesville, VA 22904, USA*

(Received 2026 February 6; Revised; Accepted)

Submitted to Planetary Science Journal

ABSTRACT

The 2023 perihelion passage of comet C/2022 E3 (ZTF) afforded an opportunity to measure the abundances and spatial distributions of coma volatiles in an Oort cloud comet at high spatial resolution near its close approach to Earth ($\Delta_{\min} \sim 0.28$ au on UT February 1). We conducted near-infrared spectroscopic observations of C/2022 E3 (ZTF) using iSHELL at the NASA Infrared Telescope Facility on UT 2023 February 9. Our measurements securely detected fluorescent emission from H₂O, CO, OCS, CH₃OH, CH₄, C₂H₆, C₂H₂, and HCN. For each instrumental setting we took exposures with the slit oriented parallel and also perpendicular to the projected Sun-comet vector, thereby enabling a test of the spatial distributions of these molecules. We report rotational temperatures, production rates, and abundance ratios (i.e., mixing ratios) for all sampled species. Our measurements found that molecular abundances in C/2022 E3 were depleted compared to their average values in Oort cloud comets with the exception of OCS, which was consistent. The H₂O production rate varied significantly and was likely tied to nucleus rotation effects. Measurements at the two slit orientations showed distinct column density and rotational temperature profiles for H₂O. Peak temperatures occurred off-nucleus and slower cooling was present in the anti-sunward hemisphere, consistent with the presence of icy grain sublimation in the coma.

Keywords: Molecular spectroscopy (2095) — High resolution spectroscopy (2096) — Near infrared astronomy (1093) — Comae (271) — Comets (280)

Corresponding author: Nathan X. Roth
nathaniel.x.roth@nasa.gov

* Visiting Astronomer at the Infrared Telescope Facility, which is operated by the University of Hawaii under contract NNH14CK55B with the National Aeronautics and Space Administration.

1. INTRODUCTION

Remote sensing of cometary atmospheres provides a window into the chemistry and physics that were preserved in their nuclei from the nascent solar system (Bockelée-Morvan et al. 2004; Dello Russo et al. 2016a). In particular, measurements with state-of-the-art long-slit infrared spectrographs, such as iSHELL at the NASA Infrared Telescope Facility (IRTF), enable spatial-spectral studies of coma chemistry. Molecular production rates (and relative abundances) and rotational temperatures for a suite of species can be retrieved by sampling multiple ro-vibrational transitions simultaneously with iSHELL’s cross-dispersed capabilities (DiSanti et al. 2017; Faggi et al. 2019). Characterizing the trends in emission intensity along the 15'' long slit reveals the projected spatial distribution of each molecule in the coma and affords the opportunity to test coma thermal physics by mapping variations in rotational temperature with nucleocentric distance (Boney et al. 2013, 2014).

The close approach of comet C/2022 E3 (ZTF; hereafter E3) in 2023 February was an excellent case for such a study. Owing to its intrinsic brightness and anticipated close approach to Earth, E3 was studied from the radio to the optical, including with ALMA and JWST (Foster et al. 2026). Its minimum geocentric distance (Δ) of 0.28 au on 2023 February 1 enabled studies of the distributions of molecular abundances and temperatures in its inner coma (~ 750 km from the nucleus). Here we report observations of E3 on 2023 February 9 taken at a heliocentric distance (r_H) of 1.12 au and $\Delta = 0.38$ au. We detected emission from H₂O, CO, OCS, CH₃OH, CH₄, C₂H₆, C₂H₂, HCN, and OH* (prompt emission). The high geocentric velocity of the comet ($d\Delta/dt \sim 38$ km s⁻¹) enabled measures of the hypervolatile species CO and CH₄ by Doppler shifting their emissions away from (highly opaque) telluric cores to regions of favorable atmospheric transmittance. We performed compositional studies of E3 using three iSHELL instrument settings. We performed multiple integrations for each setting, alternating the orientation of the slit between position angles parallel and perpendicular to the projected Sun-comet line. We provide molecular production rates, abundances, and rotational temperatures for each detected species. We provide spatial profiles of molecular emission along the slit for H₂O, HCN, CO, C₂H₆, and CH₄, and of variations in rotational temperature along the slit for H₂O. In Section 2 we detail our observations and data reduction. In Section 3 we present our results. In Section 4 we discuss the implications of our results for comet E3 and place them into context with the larger comet population.

2. OBSERVATIONS AND DATA REDUCTION

E3 is an Oort cloud comet (OCC) that reached perihelion ($q = 1.11$ au) on UT 2023 January 12. As part of a larger observing campaign throughout 2023 January and February, we targeted E3 on 2023 February 9 with the high-resolution, near-infrared facility spectrograph iSHELL (Rayner et al. 2022) at the 3 m NASA-IRTF to characterize its volatile composition. The observing log is shown in Table 1. We utilized the Lp1 and M2 iSHELL settings, along with a custom L-band setting spanning 2.81-3.09 μm (see Table 1), so as to fully sample a suite of molecular abundances. We alternated the orientation of the slit between successive observations of a given instrumental setting.

Observations were performed with a 6 pixel (0''.75) wide slit with resolving power ($\lambda/\Delta\lambda$) $\sim 4.5 \times 10^4$. We used a standard ABBA nod pattern in which the telescope is nodded along the slit between successive exposures, thereby placing the comet at two distinct positions along the slit (“A” and “B”) in order to facilitate sky subtraction. The A and B beams were symmetrically placed about the midpoint along the 15'' long slit and separated by half its length. E3 was bright and easily acquired with iSHELL’s near-infrared active guiding system. Combining spectra of the nodded beams as A-B-B+A canceled emissions from thermal background, instrumental biases, and sky emission (lines and continuum) to second order in air mass. Flux calibration was performed using an appropriately placed bright infrared flux standard star using a wide (4''.0) slit.

We employed data reduction procedures that have been rigorously tested and are described extensively in the refereed literature (Boney 2005; DiSanti et al. 2006, 2014; Villanueva et al. 2009; Radeva et al. 2010), including their application to unique aspects of iSHELL spectra (DiSanti et al. 2017; Roth et al. 2020). Each echelle order within an iSHELL setting was processed individually as previously described, such that each row corresponded to a unique position along the slit, and each column to a unique wavelength. Spectra were extracted from the processed frames by summing the signal over 15 rows (approximately 2''.5), seven rows to each side of the nucleus, defined as the peak of dust emission in a given spectral order.

We determined contributions from continuum and gaseous emissions in comet spectra as previously described (e.g., DiSanti et al. 2016, 2017) and illustrate the procedure in Figure 1. We retrieved burdens of telluric absorbers using the NASA Planetary Spectrum Generator (PSG; Villanueva et al. 2018). We convolved the fully resolved transmittance function to the resolving power of the data ($\sim 4.5 \times 10^4$) and scaled it to the level of the comet continuum. We then

Table 1. Observing Log

UT Time	Setting	Target	T_{int} (min)	r_{H} (au)	Δ (au)	$d\Delta/dt$ (km s ⁻¹)	Molecules Sampled	Slit PA (°)
UT 2023 February 9								
03:07 – 03:52	L-Custom	E3	40	1.197	0.375	37.4	H ₂ O, HCN, C ₂ H ₂ , OH*	88
04:10 – 04:44			40	1.197	0.376	37.6		178
05:08 – 05:21		BS-1040	–	–	–	–	–	–
05:22 – 05:37	Lp1	BS-1040	–	–	–	–	–	–
05:38 – 05:50	M2	BS-1040	–	–	–	–	–	–
05:54 – 06:41		E3	40	1.198	0.378	38.0	H ₂ O, CO, OCS, CN	88
06:54 – 07:41		E3	40	1.198	0.379	38.2		178
07:55 – 08:40	Lp1	E3	40	1.198	0.379	38.4	C ₂ H ₆ , CH ₃ OH, CH ₄ , OH*	178
08:47 – 09:32			40	1.198	0.380	38.6		88
09:39 – 10:15			32	1.199	0.381	38.7		178
10:25 – 10:34		BS-2560	–	–	–	–	–	–
10:41 – 10:49	M2	BS-2560	–	–	–	–	–	–
10:56 – 11:02	L-Custom	BS-2560	–	–	–	–	–	–

NOTE— r_{H} , Δ , and $d\Delta/dt$ are the heliocentric distance, geocentric distance, and geocentric velocity, respectively, of E3 at the time of observations. T_{int} is the integrated time on-source. L-Custom is a custom iSHELL setting spanning 2.81 – 3.09 μm . The solar phase angle (ϕ) was 48°. Seeing was $\sim 0''.7$.

subtracted the modeled continuum to isolate cometary emission lines and compared synthetic models of fluorescent emission for each targeted species to the observed line intensities.

Nucleocentric (or nucleus-centered) production rates (Q_{NC}) were determined using a well-documented formalism (Dello Russo et al. 1998; DiSanti et al. 2001; Bonev 2005; Villanueva et al. 2011a); see Section 3.2.2 of DiSanti et al. (2016) for further details. The Q_{NC} were multiplied by an appropriate growth factor (GF), determined using the Q -curve methodology (e.g., Dello Russo et al. 1998; DiSanti et al. 2001; Bonev 2005; Gibb et al. 2012) to establish total (or global) production rates (Q). The Q -curve formalism corrects for atmospheric seeing, which suppresses signal along lines of sight passing close to the nucleus owing to the use of a narrow slit, as well as for potential perpendicular drift of the comet during an exposure sequence.

We observed appropriately placed bright infrared flux standards near the beginning and at the end of the observing run so as to provide robust flux calibration and to test for changing conditions. NASA PSG fits to telluric H₂O absorption lines provided a measure of the precipitable water vapor during our flux standard observations: 0.92 mm for BS-1040 (UT 05:08–05:50) and 1.92 mm for BS-2560 (UT 10:25–11:02). This indicates that the telluric H₂O burden increased over the course of our observations. However, flux calibration factors (Γ , W/m²/cm⁻¹/(counts/s)) derived from measurements of BS-2560 at the end of the observations were only 4% lower than those derived from BS-1040 near the beginning of the observations. Given this small difference and to facilitate a uniform comparison, we applied flux calibration factors from BS-1040 to the entire data set. We also note that any change in applied flux calibration factors would only affect absolute Q 's, not molecular abundances for molecules within the same setting.

We estimate the uncertainty in Q due to flux calibration within an instrumental setting to be 3% for the L-Custom setting, 2% for the Lp1 setting, and 3% for the M2 setting based on the standard deviation of flux calibration factors (Γ) within each echelle order taken from eight exposures. We incorporated this additional uncertainty into our production rates. Global production rates for all detected molecules are listed in Table 2. GFs were determined for H₂O, HCN, CO, CH₄, C₂H₆, and CH₃OH.

2.1. *Mixing Ratios of Volatile Species*

2.1.1. *Molecular Fluorescence Analysis*

Synthetic models of fluorescent emission for each targeted species were compared to observed line intensities, after correcting each modeled g -factor (line intensity) for the monochromatic atmospheric transmittance at its Doppler-shifted wavelength (according to the geocentric velocity of the comet at the time of the observations). The g -factors used in synthetic fluorescent emission models in this study were generated with quantum mechanical models from the PSG. A Levenburg-Marquardt nonlinear minimization technique (Villanueva et al. 2008) was used to fit fluorescent emission from all species simultaneously in each echelle order, allowing for high precision results, even in spectrally crowded regions containing many spectral lines within a single instrumental resolution element. Production rates for each sampled species were determined from the appropriate fluorescence model at the rotational temperature of each molecule (Section 2.1.2).

2.1.2. *Determination of Rotational Temperature*

Rotational temperatures (T_{rot}) were determined using correlation and excitation analyses as described in Bonev (2005); Bonev et al. (2008); DiSanti et al. (2006); Villanueva et al. (2008). In general, well-constrained rotational temperatures can be determined for individual species having intrinsically bright lines and for which a sufficiently broad range of excitation energies is sampled. Utilizing the large spectral grasp of iSHELL, these conditions were satisfied in nucleus-centered spectra for H_2O , CO , OCS , CH_4 , C_2H_6 , and CH_3OH , and for off-nucleus spectra of H_2O .

Nucleus-centered rotational temperatures for a given molecule were in formal agreement within an instrumental setting. For instance, T_{rot} for H_2O in the L-custom integration measured parallel to the Sun-comet line agreed with that measured perpendicular to the Sun-comet line within 1σ , and the same was true for HCN . However, T_{rot} for H_2O showed modest variation between settings, rising from 78 ± 1 K in both L-custom observations to 87 ± 5 K and 90 ± 5 K in the M2 integrations.

In terms of the trace species, T_{rot} was nominally lower for CO (77 ± 10 K and 69 ± 7 K measured perpendicular and parallel to the Sun-comet line, respectively) and OCS (77 ± 21 K) than for H_2O measured in the M2 observations, and T_{rot} for HCN (108 ± 13 K, 116 ± 14 K measured parallel and perpendicular to the Sun-Comet line, respectively) was higher than H_2O in the L-Custom setting. T_{rot} for CH_4 and C_2H_6 were in agreement for all three Lp1 observations and with that for H_2O measured in L-custom and M2, whereas CH_3OH was nominally colder. However, all rotational temperatures agree with one another within 2σ . This is consistent with previous work demonstrating that rotational temperatures for primary species sampled at near-infrared wavelengths are generally in agreement (see for example Gibb et al. 2012; DiSanti et al. 2016, and references therein). All rotational temperatures are tabulated in Table 2.

3. RESULTS

We securely detected molecular emission from H_2O , CO , CH_4 , C_2H_6 , CH_3OH , HCN , C_2H_2 , and OH^* (prompt emission) in individual 40 minute integrations in the coma of E3. Figures 1, 2, and 3 show clear detections of multiple transitions of each detected species superimposed on the cometary continuum. By combining signal from both M2 integrations (80 minutes) simultaneously, we were also able to detect OCS (Figure 4).

3.1. *Spatial Profiles of Emission*

We were able to extract spatial profiles of emissions for H_2O (measured directly or through its proxy, OH^* ; see Bonev et al. 2006), HCN , CO , C_2H_6 , and CH_4 in E3 (Figures 5, 6, 7). Although OH^* has been established as a reliable tracer for the production and spatial distribution of its parent, H_2O , it is important to note in the context of this study that spatial profiles of the two molecules may show subtle differences, particularly in the case of H_2O sublimation from icy grains. The high brightness and small geocentric distance of E3 enabled us to map the inner coma (within ~ 750 km to either side of the nucleus) in high detail, with the $0''.167$ iSHELL spatial pixel scale subtending a projected distance of 45 km. The moderate phase angle ($\phi \sim 48^\circ$) during our observations must be considered when interpreting spatial profiles.

Spatial profiles of emission provide insights into how molecules are produced: those peaking strongly near the nucleus and falling off with $\sim \rho^{-1}$ dependence are associated with direct nucleus release, whereas molecules with a very broad, flat spatial distribution are consistent with daughter products or extended source molecules (Dello Russo et al. 2016b). For molecules produced via direct nucleus sublimation, spatial profiles reveal whether they originate from common or distinct outgassing sources on the nucleus, and in turn, whether they were associated or segregated as ices in the

Table 2. Molecular Composition of C/2022 E3 as Measured by iSHELL

Setting	Species	$T_{\text{rot}}^{\text{a}}$	GF ^b	Q^{c}	Relative Abundance	
		(K)		(10^{25} s^{-1})	$Q_{\text{x}}/Q_{\text{H}_2\text{O}}^{\text{d}}$ (%)	$Q_{\text{x}}/Q_{\text{C}_2\text{H}_6}^{\text{e}}$
UT 2023 February 9, $r_{\text{H}} = 1.197 \text{ au}$, $\Delta = 0.375 \text{ au}$						
L-Custom	H ₂ O	78 ± 1	2.21 ± 0.06	8352 ± 150	100	374 ± 11
PA = 88°	HCN	108 ± 13	2.05 ± 0.22	8.12 ± 0.53	0.097 ± 0.007	0.36 ± 0.03
	C ₂ H ₂	(78)	(2.21)	4.45 ± 0.86	0.05 ± 0.01	0.20 ± 0.04
L-Custom	H ₂ O	78 ± 1	2.38 ± 0.02	8050 ± 102	100	361 ± 9
PA = 178°	HCN	116 ± 14	1.73 ± 0.21	6.26 ± 0.53	0.078 ± 0.007	0.28 ± 0.03
	C ₂ H ₂	(78)	(2.38)	< 3.45(3 σ)	< 0.04(3 σ)	< 0.16(3 σ)
M2	H ₂ O	87 ± 5	2.03 ± 0.15	6080 ± 228	100	273 ± 13
PA = 178°	CO	77 ± 10	2.06 ± 0.15	33.3 ± 2.6	0.55 ± 0.05	1.49 ± 0.13
M2	H ₂ O	90 ± 5	2.37 ± 0.11	6629 ± 259	100	297 ± 14
PA = 88°	CO	69 ± 7	2.42 ± 0.14	35.9 ± 2.3	0.54 ± 0.04	1.61 ± 0.12
M2 ^(a)	OCS	77 ± 21	(2.03)	3.06 ± 0.53	0.046 ± 0.008	0.14 ± 0.03
Lp1	OH*	(78)	2.01 ± 0.12	7159 ± 253	100	262 ± 13
PA=178°	CH ₄	70 ± 10	2.27 ± 0.12	18.6 ± 1.3	0.26 ± 0.02	0.68 ± 0.06
	C ₂ H ₆	77 ± 7	2.54 ± 0.05	27.2 ± 0.9	0.38 ± 0.01	1
	CH ₃ OH	88 ± 17	(2.01)	58.5 ± 6.3	0.82 ± 0.04	2.15 ± 0.24
Lp1	OH*	(78)	2.77 ± 0.16	8966 ± 883	100	416 ± 43
PA=88°	CH ₄	87 ± 12	2.50 ± 0.28	25.9 ± 1.0	0.29 ± 0.03	1.20 ± 0.06
	C ₂ H ₆	70 ± 7	2.56 ± 0.08	21.5 ± 0.7	0.24 ± 0.03	1
	CH ₃ OH	64 ± 9	(2.77)	53.7 ± 4.5	0.60 ± 0.08	2.50 ± 0.22
Lp1	OH*	(78)	2.32 ± 0.15	7064 ± 352	100	339 ± 20
PA=178°	CH ₄	76 ± 13	2.58 ± 0.51	19.4 ± 1.5	0.28 ± 0.03	0.93 ± 0.08
	C ₂ H ₆	70 ± 7	2.32 ± 0.08	20.8 ± 0.6	0.30 ± 0.02	1
	CH ₃ OH	49 ± 9	(2.32)	45.4 ± 4.8	0.64 ± 0.08	2.18 ± 0.24

NOTE—^aRotational temperature. ^bGrowth factor. This represents the ratio of global Q to Q_{NC} based on the central $0''.75 \times 0''.83$ aperture having peak emission flux. ^cProduction rate. An additional uncertainty of 3%, 2%, and 3% was incorporated into Q 's for L-Custom, M2, and Lp1, respectively, based on the standard deviation of flux calibration factors (Γ , $\text{W}/\text{m}^2/\text{cm}^{-1}/(\text{count}/\text{s})$). ^dMixing ratio with respect to simultaneously measured H₂O (H₂O = 100). ^eMixing ratio with respect to C₂H₆ (C₂H₆ = 1). A weighted average $Q(\text{C}_2\text{H}_6) = (2.23 \pm 0.04) \times 10^{26} \text{ s}^{-1}$ calculated from all three Lp1 observations was used to calculate mixing ratios for the Lcustom and M2 settings, and an additional 10% uncertainty was incorporated to account for the non-simultaneous observations of C₂H₆. In the context of interpreting relative abundances, bold font emphasizes that H₂O was only directly measured in the L-Custom and M2 settings, whereas C₂H₆ was only directly measured in the Lp1 setting.

nucleus. In particular, molecules with distinct outgassing sources on the nucleus should project differently onto the slit as its orientation (position angle) is changed.

Dello Russo et al. (2022) characterized the spatial profiles in comet C/2014 Q2 (Lovejoy) using four quantities: (1) the multiplicative growth factor, (2) the difference in half width at half maximum (HWHM) of a Gaussian fit to the volatile emission profile as compared to that of co-measured dust, (3) the difference in peak pixel of the volatile emission (determined from the peak of the Gaussian fit) compared to that of co-measured dust, and (4) the symmetry of the volatile emission profile derived from the ratio of summed flux along each side of the slit (for E3, this was from $\sim 150 \text{ km}$ to $\sim 750 \text{ km}$ projected distance).

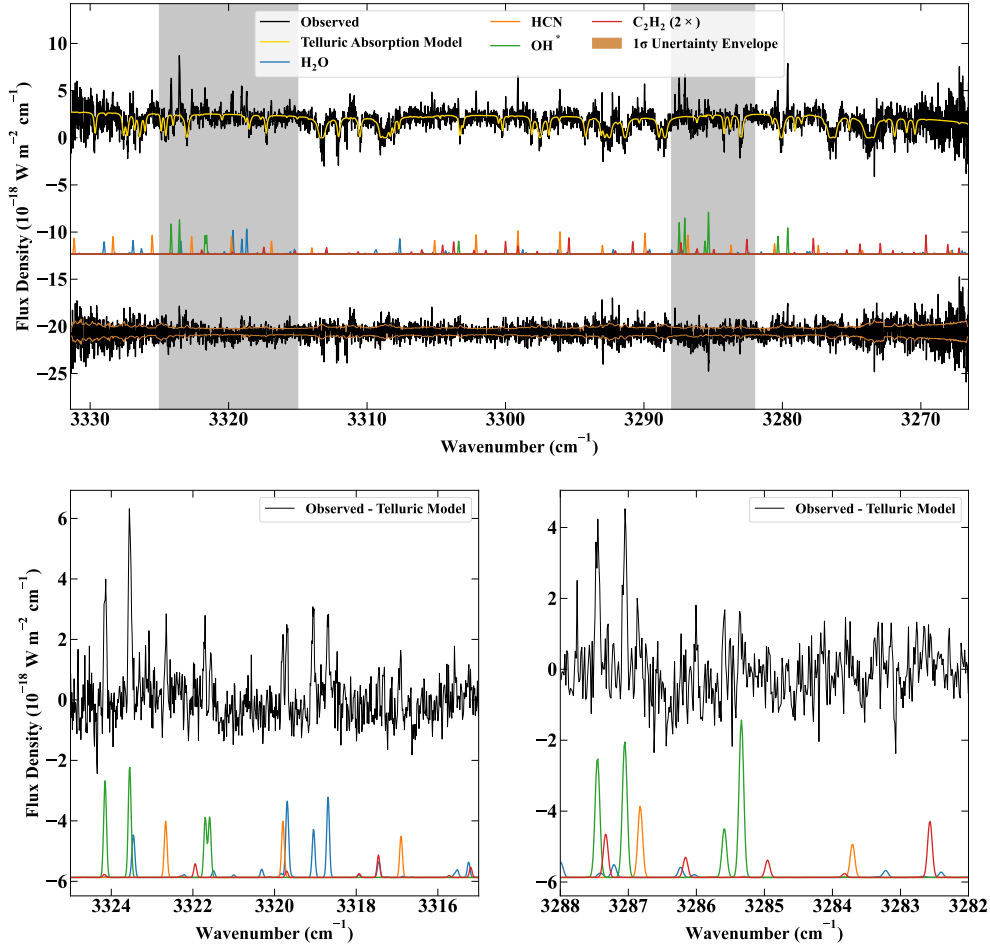


Figure 1. Upper. Detections of H₂O, HCN, C₂H₂, and OH* in E3 covering iSHELL echelle order 170–172. The uppermost trace is the observed cometary spectrum with the telluric transmittance model superimposed. Below are individual molecular fluorescence models color-coded by species. The bottom trace shows the residual (cometary spectrum minus all models) with the 1 σ uncertainty envelope overlaid and shaded. **Lower.** Zoomed plots covering the gray shaded regions indicated in the upper panel. In this case, the uppermost trace is the telluric-subtracted comet spectrum, with individual fluorescence models plotted below. We searched for NH₂, a potentially confounding species in this spectral region, but did not detect it. Our 3 σ upper limit is NH₂/H₂O < 0.03%.

We followed a similar procedure for E3; however, given the clear asymmetry of some of the profiles (HCN in particular), we instead performed least squares fitting of a skewed Gaussian to the profiles using the `SkewedGaussianModel` of the `lmfit` application. This skewed Gaussian allowed for a considerably improved fit to the profiles compared to a classical Gaussian. For measurements taken with a slit position angle oriented parallel to the projected Sun-comet line (PA = 88 $^\circ$), quantities (3) and (4) are with respect to the sunward/anti-sunward directions, whereas for a perpendicular slit position angle they are with respect to the roughly north/south directions. Our results are quantified in Table 3.

During the L-custom setting measurements along the projected Sun-comet line, H₂O emission was relatively symmetric, while being only slightly broader than and peaking co-spatially with the co-measured dust. In contrast, HCN

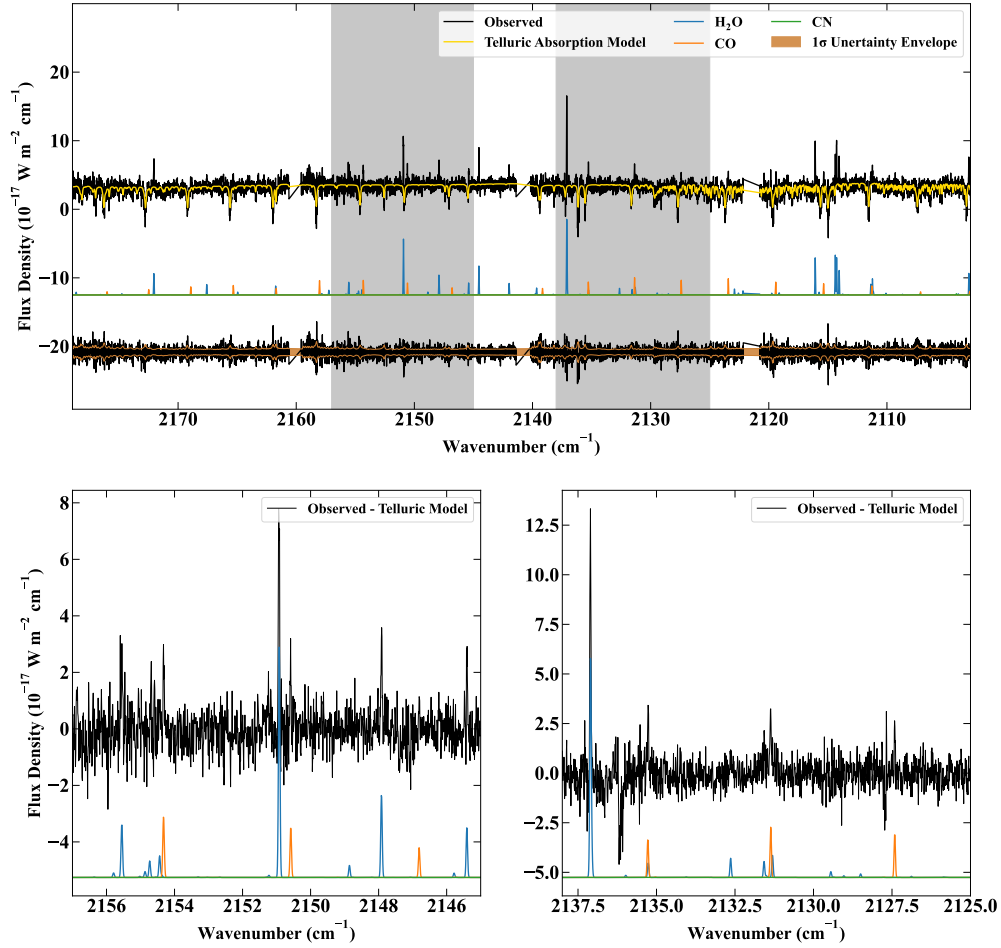


Figure 2. Upper, Lower. Detections of H₂O and CO in E3 covering iSHELL echelle orders 109–112, with traces and labels as in Figure 1.

was highly asymmetric, peaking in the anti-sunward direction while showing a sunward enhancement. When measured perpendicular to the Sun-comet line, the characteristics of the H₂O profile were largely the same, although it was more symmetric than the sunward/anti-sunward projection. Likewise, HCN continued to show considerable asymmetry, yet the sense of the asymmetry and the direction of the peak pixel offset changed. Given these significant changes in the HCN spatial profile between slit orientations (compared to the consistency of the H₂O), it is likely that the E3 displayed heterogeneous outgassing, with each molecule originating from distinct nucleus sources.

During observations with the M2 setting, H₂O and CO emission were both relatively symmetric and co-spatial with the continuum; however, H₂O peaked in the sunward direction, whereas CO peaked in the projected anti-sunward direction. During the Lp1 setting, H₂O emission (measured through its proxy, OH* prompt emission) was co-spatial with the dust during the first measurement perpendicular to the Sun-comet line and also the measurement parallel to it. However, it drifted considerably from the continuum during the second perpendicular measurement. These differences are notable in the context of spatial profiles of H₂O and OH* measured in C/2014 Q2 Lovejoy, where H₂O peaked co-spatially with and was only slightly broader than the dust, whereas the OH* profiles showed an anti-sunward offset and broader profiles compared to the dust (Dello Russo et al. 2022). Similarly, C₂H₆ showed changes, being

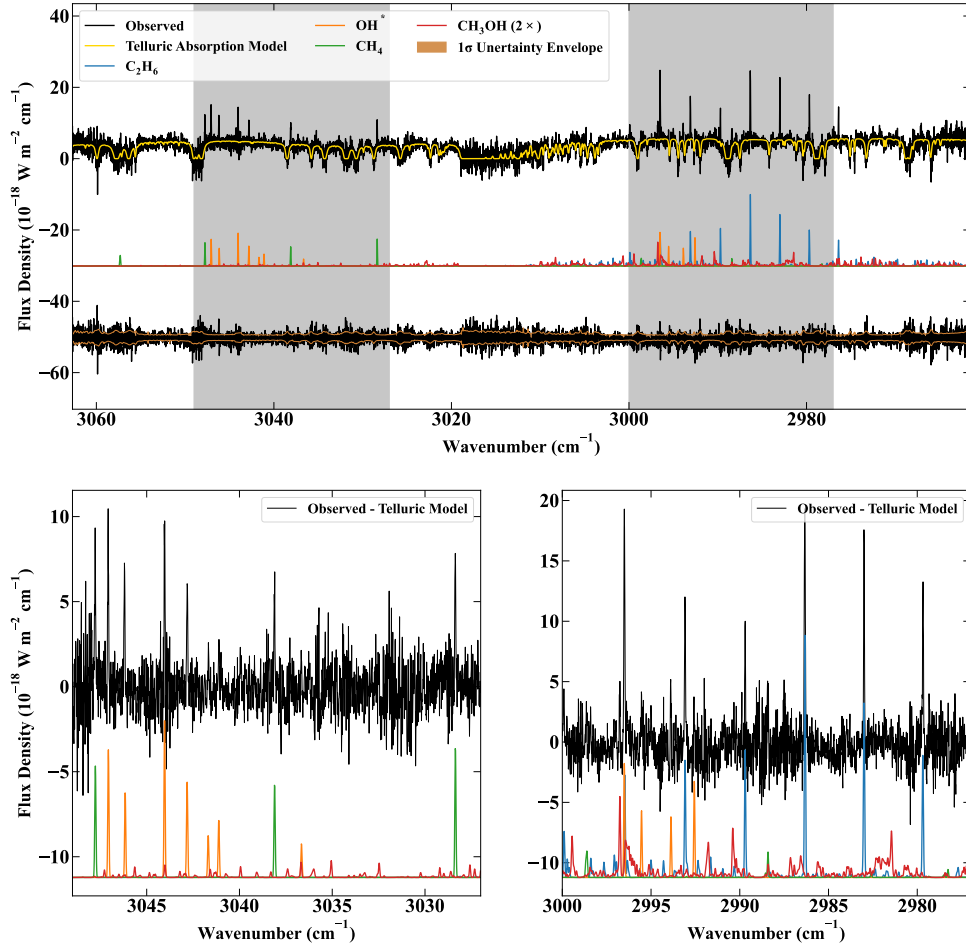


Figure 3. Upper, Lower. Detections of H_2O (OH^*), C_2H_6 , CH_3OH , and CH_4 in E3 covering iSHELL echelle orders 154–158, with traces and labels as in Figure 1.

broader than H_2O during the first perpendicular measurement yet narrower than it in the second, and its asymmetry also changed. In contrast, CH_4 was co-spatial with the dust and relatively symmetric in all instances. Overall, these spatial profiles suggest common outgassing sources for H_2O , CO , and CH_4 , whereas HCN and potentially C_2H_6 may have had distinct sources.

3.2. Spatial Profiles of H_2O Rotational Temperature

Trends in rotational temperature along the slit can be tested for molecules with sufficiently high signal-to-noise at off-nucleus positions. For E3, this was satisfied for H_2O . We extracted spectra in sliding 1-pixel ($0''.167$) extracts along the slit and retrieved molecular column density and rotational temperature at each position. Figure 8 shows all H_2O transitions detected in a nucleus-centered extract of a single 40 minute on-source integration, and Figure 9 shows the extracted column density and rotational temperature profiles.

The rotational temperature profiles for each slit orientation are distinct and asymmetric about the nucleus position. The temperature profile measured along the projected Sun-comet line is 84 ± 2 K at the nucleus position and rises to 88 ± 2 K at ~ 135 km off-nucleus in the anti-sunward direction. Although the temperature in the projected sunward

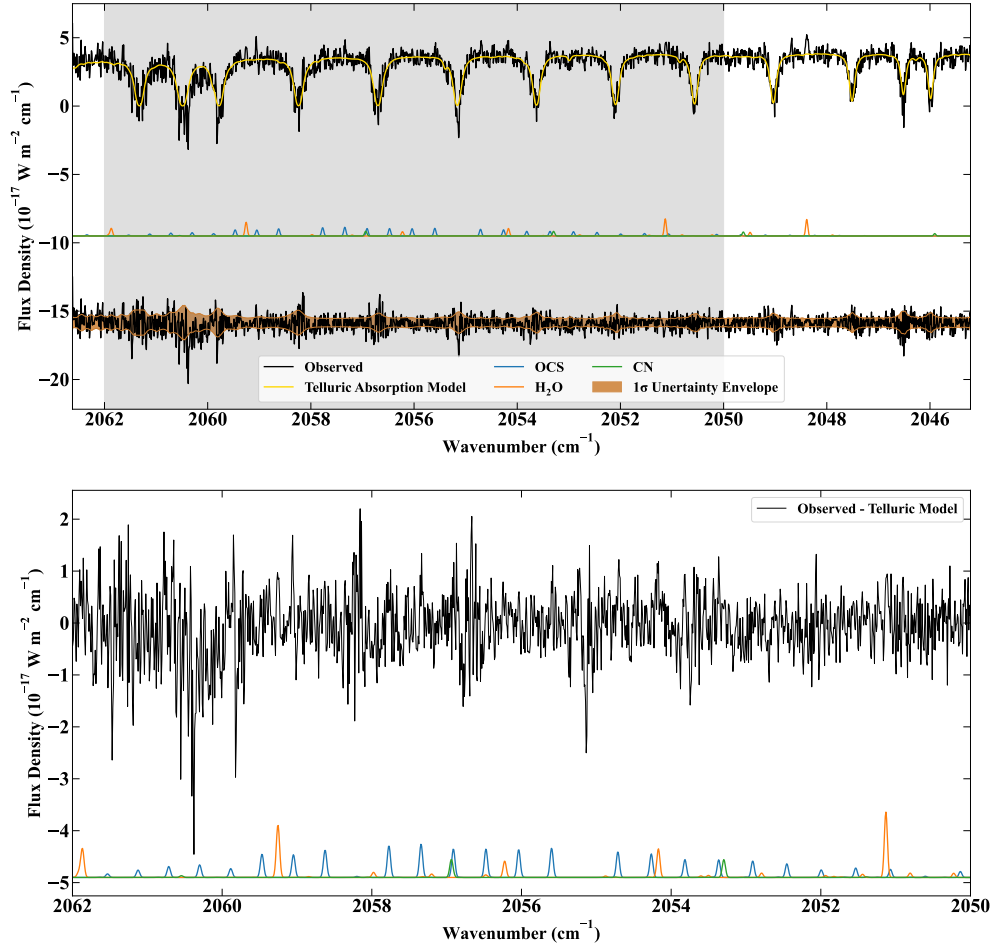


Figure 4. Upper, Lower. Detections of H₂O, OCS, and CN in E3 covering iSHELL echelle order 106, with traces and labels as in Figure 1.

side falls to ~ 65 K within 320 km, the temperature in the anti-sunward side does not reach the same value until nearly 550 km from the nucleus.

The temperature profile measured perpendicular to the projected Sun-comet line is also remarkable, rising from 80 ± 1 K at the nucleus position to 84 ± 1 K at 90 km north of the nucleus before beginning to decrease. There is also a difference in heating between the northern and southern hemispheres, with the north side cooling to 66 ± 2 K within 270 km of the nucleus, whereas the southern hemisphere doesn't reach the same value until 410 km from the nucleus. Collectively, these results indicate significant differences in the balance of heating and cooling mechanisms in the day and night sides of the coma.

4. DISCUSSION

Our measurements of E3 detail its complex coma, revealing distinct sources of outgassing for different species, asymmetric coma temperature profiles, and molecular abundances for multiple species. We address each of these topics, compare our measurements against those in other studies of E3, and place our results into context with the comet population.

Table 3. Emission Spatial Profile Characteristics in C/2022 E3

Setting/Orientation	Molecule	GF ^(a)	Differences (Volatiles - Dust)		Asymmetry ^(d)
			HWHM ^(b) (pixels)	Peak Position ^(c) (pixels)	
L-Custom	H ₂ O	2.21 ± 0.06	0.50 ± 0.61	-0.22 ± 0.94	0.76 ± 0.03
PA = 88°	HCN	2.05 ± 0.22	0.00 ± 0.62	2.61 ± 0.99	5.69 ± 0.75
L-Custom	H ₂ O	2.38 ± 0.02	0.50 ± 0.56	0.08 ± 0.78	1.00 ± 0.01
PA = 178°	HCN	1.73 ± 0.21	-1.50 ± 0.67	-2.48 ± 0.87	0.20 ± 0.03
M2	H ₂ O	2.03 ± 0.15	0.50 ± 0.64	-0.99 ± 0.82	0.63 ± 0.04
PA = 178°	CO	2.06 ± 0.15	1.00 ± 0.83	-0.10 ± 1.09	1.29 ± 0.03
M2	H ₂ O	2.37 ± 0.11	1.00 ± 0.86	0.47 ± 1.26	1.09 ± 0.05
PA = 88°	CO	2.42 ± 0.14	1.50 ± 0.76	-0.78 ± 1.06	0.63 ± 0.02
Lp1	H ₂ O (OH*)	2.01 ± 0.12	1.00 ± 1.02	0.12 ± 1.64	0.82 ± 0.03
PA = 178°	CH ₄	2.27 ± 0.12	1.00 ± 0.85	-0.02 ± 1.51	1.41 ± 0.04
	C ₂ H ₆	2.54 ± 0.05	1.50 ± 0.73	0.83 ± 1.27	0.93 ± 0.02
Lp1	H ₂ O (OH*)	2.77 ± 0.15	0.50 ± 1.08	0.60 ± 1.71	0.50 ± 0.01
PA = 88°	CH ₄	2.50 ± 0.28	0.50 ± 1.34	-0.59 ± 2.24	0.83 ± 0.03
	C ₂ H ₆	2.56 ± 0.08	0.50 ± 1.33	-0.10 ± 1.98	0.78 ± 0.03
Lp1	H ₂ O (OH*)	2.32 ± 0.15	0.00 ± 1.60	2.24 ± 3.89	1.09 ± 0.03
PA = 178°	C ₂ H ₆	2.32 ± 0.08	-0.50 ± 1.81	1.37 ± 4.06	0.46 ± 0.03

NOTE—^aGrowth factor. This represents the ratio of global Q to Q_{NC} based on the central $0''.75 \times 0''.83$ aperture having peak emission flux. ^bDifference in spatial profile full width at half maximum between volatile emission and co-measured in dust (1 pixel represents a projected distance at the comet of 45 km). Positive values correspond to a broader volatile profile compared to the dust, whereas negative values indicate a narrower profile. ^cDifference between the spatial profile peak position between volatile emission and co-measured dust. For measurements taken along the projected Sun-comet vector (PA = 88°), positive values correspond to a sunward (westward) volatile shift, whereas for measurements taken perpendicular (PA = 178°), positive values correspond to a northward volatile shift. ^dSymmetry of the profile as measured by the ratio of flux along each side of the slit, excluding the central 5 pixels around the peak flux position.

4.1. Molecular Abundances in C/2022 E3

Our measurements in C/2022 E3 provide a record of its coma composition over ~ 7 hours near its closest approach to Earth. On the one hand, overall coma activity varied significantly, with $Q(\text{H}_2\text{O})$ falling nearly 30% from its value during our first Lcustom block (UT 03:07–03:52) to its value during the first M2 integration (UT 05:38–05:50), then rising nearly the same amount by the second Lp1 block (UT 08:47–09:32; Table 2). On the other hand, the relative molecular abundances for HCN, CO, and CH₄ agreed within 2σ uncertainty for all integrations of a given instrumental setting. In this context, it is also interesting to emphasize that despite clear evidence for heterogenous outgassing of HCN and H₂O, their relative molecular abundances differed by $< 2\sigma$ uncertainty between the first and second L-Custom integrations. This scenario of flat molecular abundances despite complex outgassing patterns and changing slit orientations is consistent with results seen in EPOXI target 103P/Hartley 2 (Dello Russo et al. 2011; Mumma et al. 2011; Kawakita et al. 2013).

In contrast, CH₃OH and C₂H₆ abundances decreased by 30% and 45%, respectively, between the first and second Lp1 observations before moderately increasing during the third. The trend in CH₃OH/H₂O and C₂H₆/H₂O can be explained in terms of a continuous decrease in $Q(\text{CH}_3\text{OH})$ and $Q(\text{C}_2\text{H}_6)$ across the entire Lp1 sequence while $Q(\text{H}_2\text{O})$ cycled up and down. On the other hand, despite significant variation in the CH₄/C₂H₆ abundances, CH₃OH/C₂H₆ remained constant within uncertainty. It is therefore appropriate to recall that H₂O was not measured directly in the Lp1 setting (rather through its proxy, OH*), and that overall, relative abundances of molecules measured

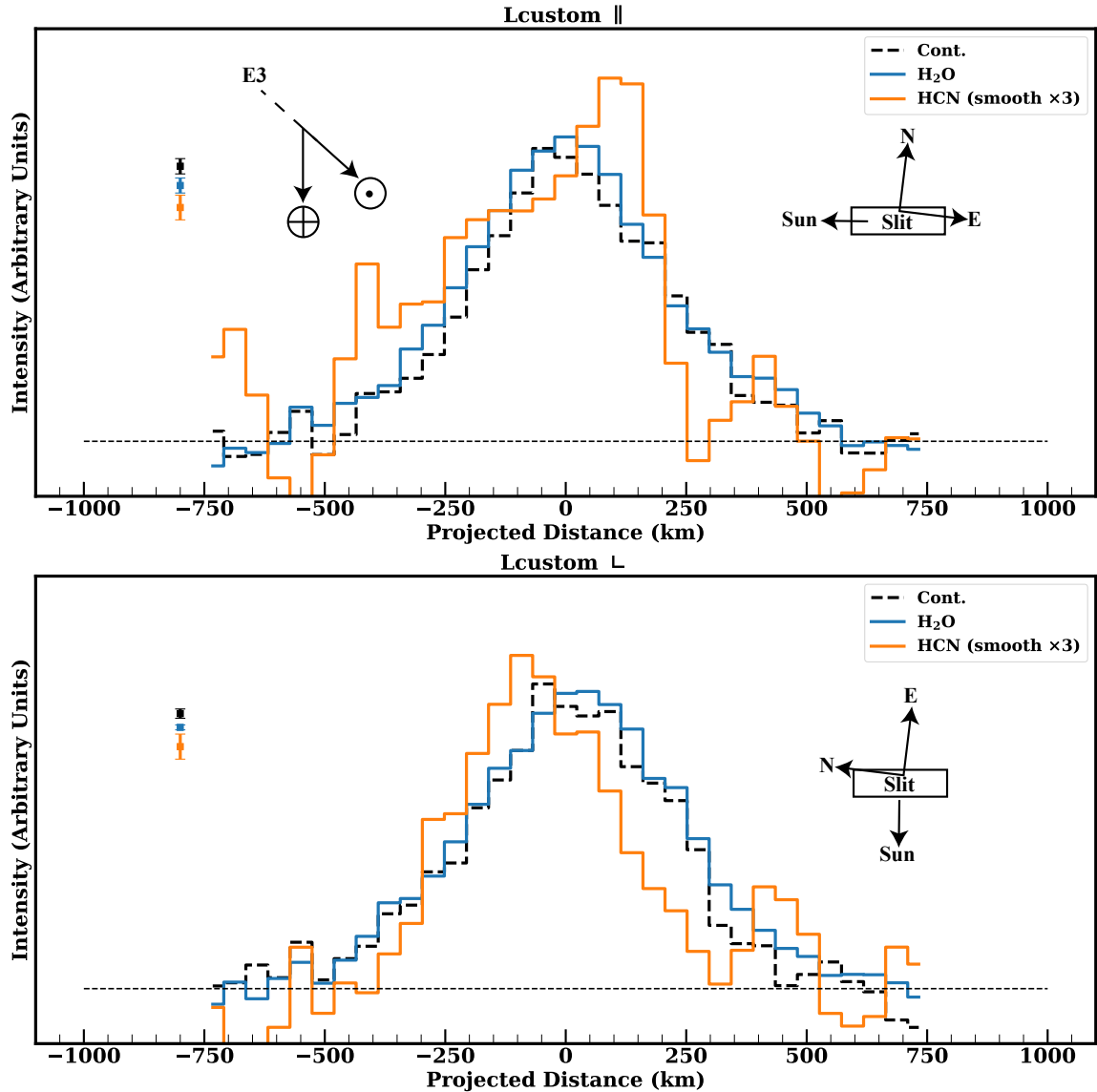


Figure 5. Upper. Spatial profiles of emissions for co-measured H₂O (blue), HCN (orange), and continuum (dashed) in E3. Color-coded 1σ uncertainties are shown for the profile of each species. The slit was oriented along the projected Sun-comet line (position angle 88°), with the Sun-facing direction to the left as indicated. Also shown is the Sun-comet-Earth angle (phase angle, β) of 48° . “Smooth” indicates the width (pixels) of a boxcar smoothing kernel applied to HCN. **Lower.** Spatial profiles of co-measured H₂O, HCN, and continuum in E3 with the slit oriented perpendicular to the projected Sun-comet line (position angle 178°).

simultaneously within a setting (i.e., HCN, CO, C₂H₂, and H₂O; CH₃OH, and CH₄) showed the most consistency across time and are likely the most robust.

Despite the uncertainties, it is possible that the variation in $Q(\text{H}_2\text{O})$ was tied to rotational effects, as our lowest values coincide with measurements taken halfway through its ~ 8 hour rotational period (Manzini et al. 2023; Knight et al. 2023), with different active sites rotating into and out of the dayside hemisphere and dominating activity. Foster et al. (2026) found evidence for such variations in $Q(\text{H}_2\text{O})$ through spatial-spectral mapping of H₂O with JWST roughly one month after this study. Observations at radio wavelengths produced similar results, with Biver et al. (2024a) reporting variations in H₂O and CH₃OH production rates with an 8–9 hour period, and Li et al. (2025) finding that HCN was temporally variable as well.

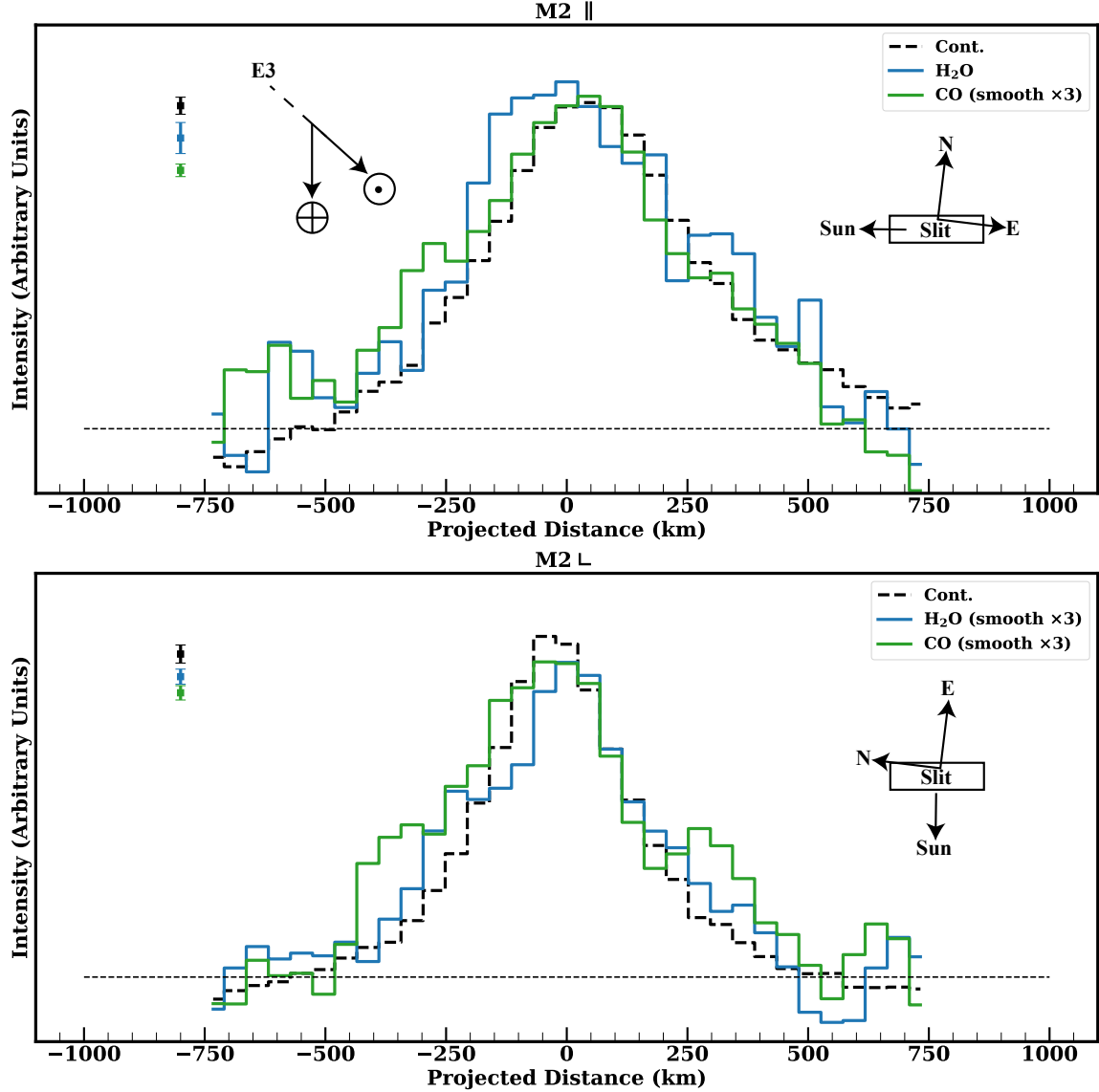


Figure 6. **Upper.** Spatial profiles of emissions for co-measured H₂O (blue), CO (green), and continuum (dashed) in E3, with traces and labels as in Figure 5. The slit was oriented along the projected Sun-comet line. **Lower.** Spatial profiles of co-measured H₂O, CO, and continuum in E3 with the slit oriented perpendicular to the projected Sun-comet line.

We can also compare our molecular abundances against those found for E3 in other studies at infrared and radio wavelengths. Our abundances for HCN and CO are in formal agreement with those found by [Biver et al. \(2024a\)](#), but lower than those reported in [Li et al. \(2025\)](#), and both molecules are considerably depleted with respect to average values in measured Oort cloud comets ([Dello Russo et al. 2016a](#)). It is interesting to note that HCN abundances in a given comet often disagree between radio and infrared measurements (by up to a factor of 6; [Biver et al. 2024b](#)), and E3 is an uncommon example of good agreement. On the other hand, our CH₃OH abundance is lower by a factor of ~ 2 –3 than that reported by [Biver et al. \(2024a\)](#) and a factor ~ 1.7 than [Foster et al. \(2026\)](#), yet all values are depleted compared to average values in Oort cloud comets ([Dello Russo et al. 2016a](#)). Conversely, our OCS abundance is twice as high as [Biver et al. \(2024a\)](#) yet in agreement with [Foster et al. \(2026\)](#), and consistent with its mean value among measured comets ([Saki et al. 2020](#)).

As radio observations cannot sample the symmetric hydrocarbons, which lack a rotational dipole moment, our study provides their sole report in E3 to date. Our C₂H₆, CH₄, and C₂H₂ abundances are all depleted compared to their mean abundances among measured Oort cloud comets ([Dello Russo et al. 2016a](#)).

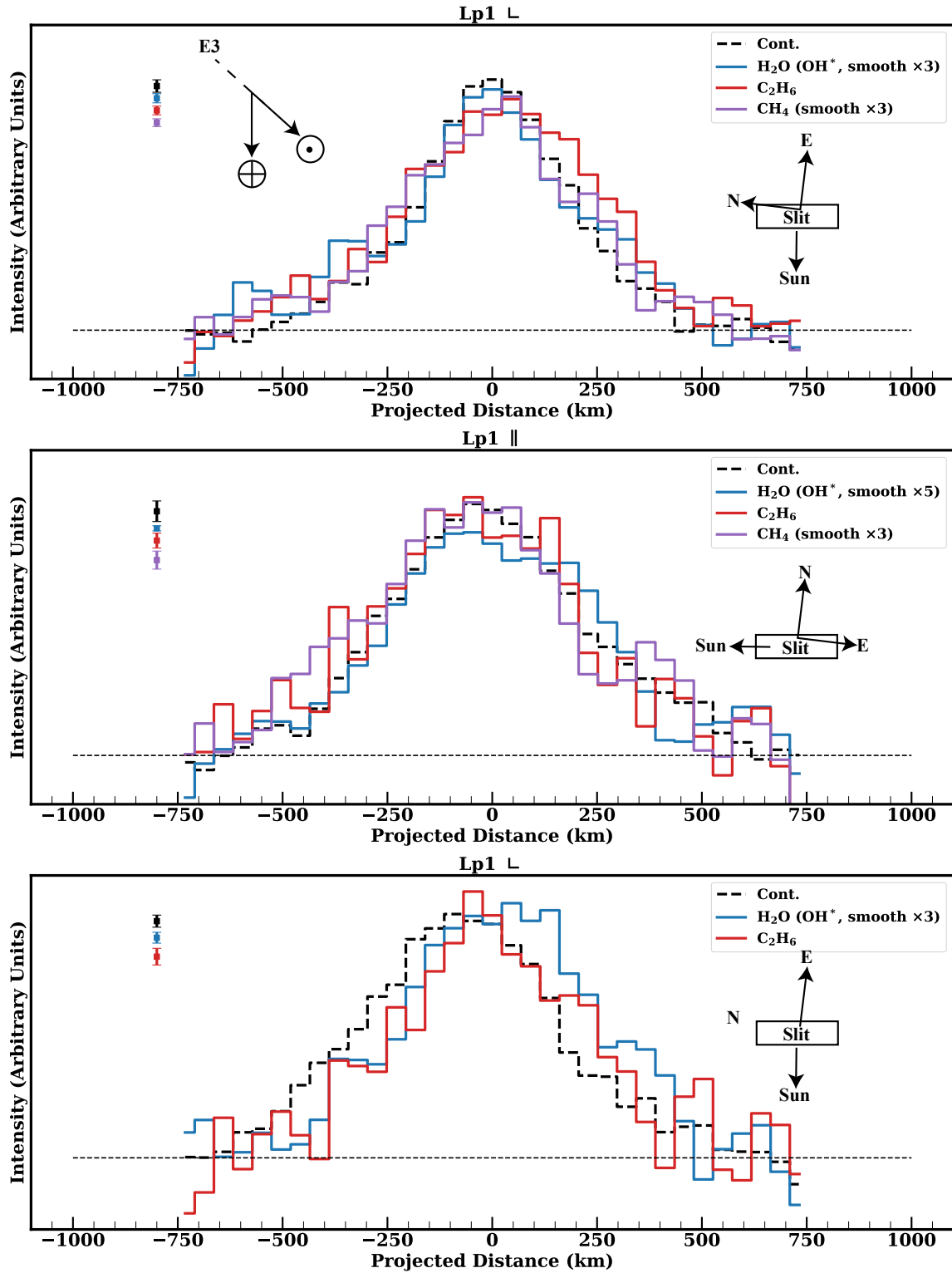


Figure 7. Upper. Spatial profiles of emissions for co-measured H₂O (OH*, blue), C₂H₆ (red), CH₄ (purple), and continuum (dashed) in E3, with traces and labels as in Figure 5. The slit was oriented perpendicular to the Sun-comet line (first integration, UT 07:55 - 08:40). **Middle.** Spatial profiles of H₂O, C₂H₆, CH₄ and continuum in E3 with the slit oriented along the projected Sun-comet line. **Lower.** Spatial profiles of H₂O, C₂H₆, CH₄ and continuum in E3 with the slit oriented perpendicular to the projected Sun-comet line (third integration, UT 09:39 - 10:15).

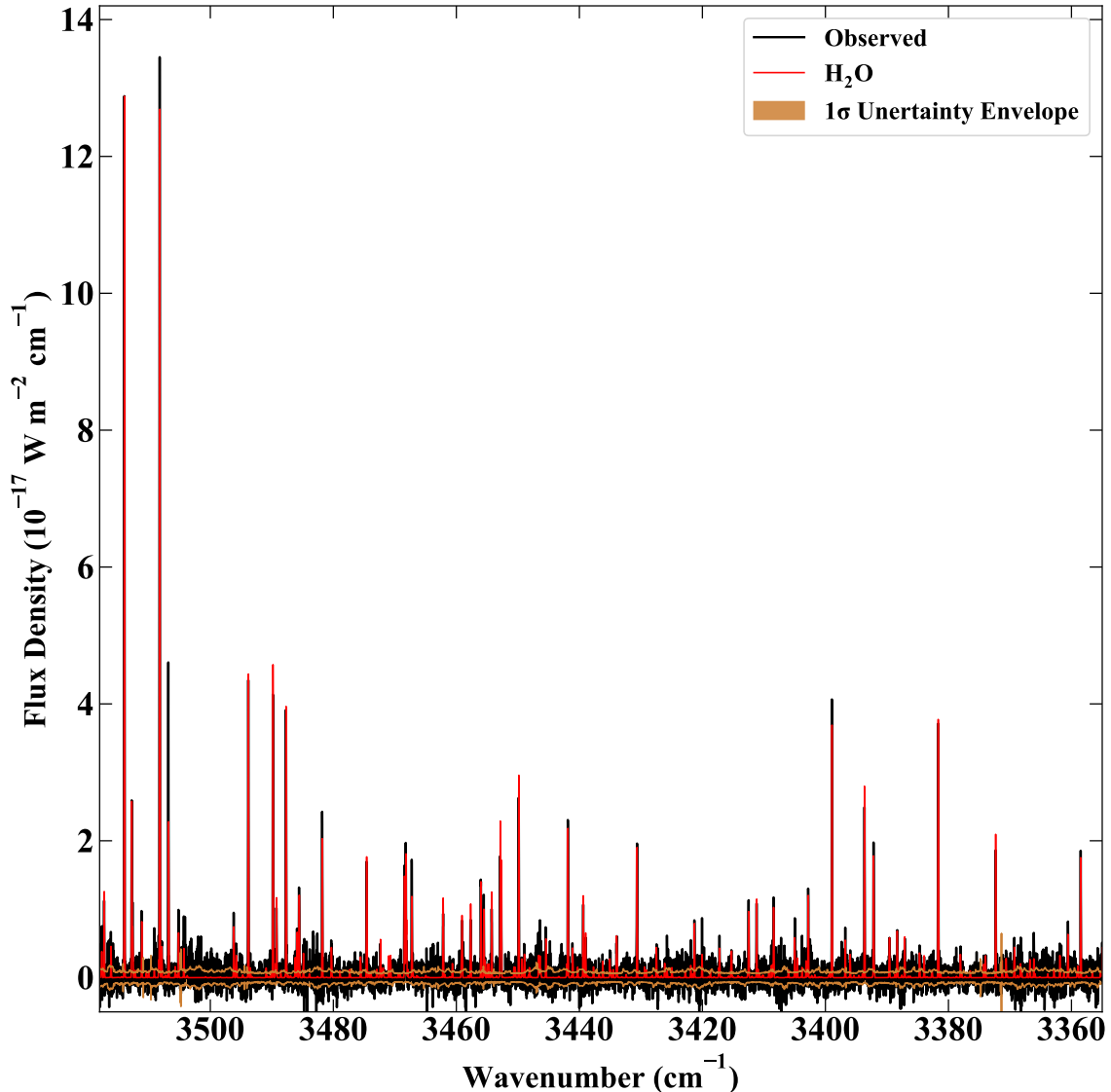


Figure 8. Detections of H₂O in E3 covering iSHELL echelle orders 174–182. The best-fit fluorescence model is overlaid in red, and the 1 σ uncertainty envelope is shaded in bronze.

4.2. Coma Thermal Physics in C/2022 E3

Our H₂O rotational temperature profiles (Figure 9) measured at distinct position angles in the coma provide a window into the coma physics of E3. The rotational temperature profiles did not track the column density profiles in either slit orientation, and in each case distinct hemispheric asymmetries were observed, with the rotational temperature peaking off-nucleus and cooling occurring significantly slower in one hemisphere. In particular, the profile measured parallel to the Sun-comet line was cooler and decreased more quickly in the projected sunward direction, while peaking off-nucleus and cooling more slowly in the anti-sunward side. The disparity in peak position between the H₂O rotational temperature and column density profiles measured parallel to the Sun-comet line is consistent with the effects of icy grains being dragged by radiation pressure into the anti-sunward hemisphere before releasing their H₂O at an elevated T_{rot} (namely the vacuum sublimation temperature of H₂O). This interpretation is also consistent with the double-peaked temperature profile measured perpendicular to the Sun-comet line, where the anti-sunward, off-nucleus rise in rotational temperature is projected symmetrically along the line of sight in the north and south directions.

These results are similar to those found in ground-based observations of EPOXI target 103P/Hartley 2 (Bonev et al. 2013), with the H₂O rotational temperature profile along the Sun-comet line decoupled from the column density profile

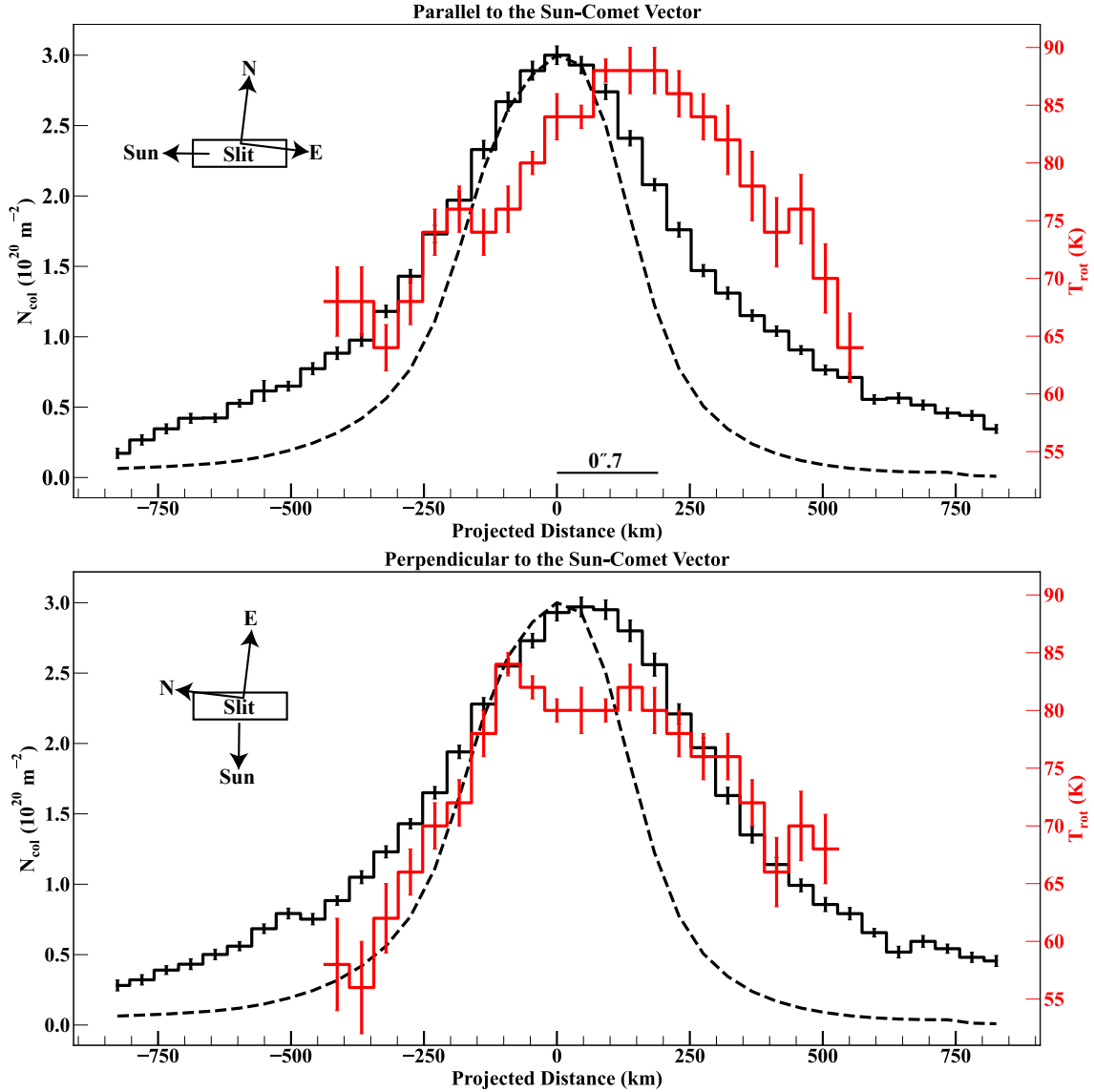


Figure 9. Left. Spatial profiles of column density (black) and rotational temperature (red) for H_2O in E3 with the slit positioned along the projected Sun-comet line. The stellar PSF (dashed) is also shown, along with the orientation of the slit. The black bar indicates the $0''.7$ seeing. **Right.** Spatial profiles of H_2O column density and rotational temperature in E3 with the slit oriented perpendicular to the projected Sun-comet line.

and an increase in temperature in the anti-sunward direction. Measurements by the EPOXI spacecraft demonstrated a complex outgassing geometry originating from the nucleus of 103P/Hartley 2, with icy H_2O -coated grains dragged into the coma from the waist region before sublimating and adding to the coma water content. This synergy between ground- and space-based results provided strong evidence for the diagnostic signature of icy grain sublimation in high-resolution ground-based spectroscopy as reported here for E3.

Our results are also consistent with those found in comet 46P/Wirtanen at radio wavelengths using single dish spectroscopy (Biver et al. 2021) and interferometric imaging with the ALMA array (Cordiner et al. 2023), which were explained by the combined effects of more efficient adiabatic cooling in the dayward side and the heating effects of sublimation from icy grains in the anti-sunward side. It is important to note that both 103P/Hartley 2 and 46P/Wirtanen were hyperactive comets, with their overabundant H_2O production relative to their small nucleus size attributed to icy grain sublimation in the coma.

To further test the likelihood of icy grain sublimation in E3, we worked to determine whether it was a hyperactive comet like 46P/Wirtanen or 103P/Hartley 2. A hyperactive comet is defined as having a nucleus active fraction greater than 100%. Liu & Liu (2024) found a lower limit to E3’s nucleus size of 0.87 km and an upper limit of 2.79 km. We calculated the H₂O active fractional area for E3 using the sublimation model of Cowan & A’Hearn (1979) for a visual albedo of 0.05 and an infrared emissivity of 0.95. We used the Small-Bodies-Node/ice-sublimation code (Van Selous & Kelley 2021) to calculate the average H₂O sublimation rate per surface unit, Z , at $r_H = 1.05$ au. We used the absolute mean $Q(\text{H}_2\text{O})$ during our observations of $(7.5 \pm 0.9) \times 10^{28} \text{ s}^{-1}$. The active area is calculated by dividing $Q(\text{H}_2\text{O})$ by Z , and the nucleus active fractional area is found by dividing the active area by the nucleus surface area. We find $Z = 3.25 \times 10^{17} \text{ mol cm}^{-2} \text{ s}^{-1}$. For a nucleus radius of 2.79 km and our $Q(\text{H}_2\text{O})$, this corresponds to an active fraction of 28%, whereas for a 0.87 km nucleus radius the active fraction is 279%. Indeed, if E3’s nucleus radius were smaller than 1.35 km, it would be a hyperactive comet during our observations. Combined with our rotational temperature and column density profiles, this is another line of evidence that icy grain sublimation likely played a significant role in E3’s coma near its closest approach to Earth.

However, the thermal physics of E3’s coma did not necessarily remain constant with time. Foster et al. (2026) also found generally higher rotational temperatures in the projected anti-sunward hemisphere of E3 roughly one month (2023 March 1 - 4) after the observations reported here. This sunward/anti-sunward dichotomy was seen for both H₂O (measured with JWST NIRSpec IFU observations) as well as CH₃OH (measured with ALMA), with both instruments sampling gas within ~ 1000 km projected distance from the nucleus. The higher anti-sunward temperature was explained as a consequence of more efficient adiabatic cooling in the sunward hemisphere. However, their observations showed a continuous decrease of the rotational temperature with distance in both the projected sunward and anti-sunward hemispheres, without any evidence for an off-nucleus increase in temperature. Thus, it is possible that icy grain sublimation was not a constant effect in E3’s coma.

Aside from icy grain sublimation, off-nucleus increases in temperature may also be explained by the effects of electron collisional heating (Biver et al. 1999; Cordiner et al. 2025). However, Foster et al. (2026) demonstrated through detailed radiative transfer modeling that such heating should have taken place near the electron contact surface at roughly 750 km projected distance from the nucleus for E3. This is considerably more distant than the off-nucleus temperature increases in this work, which occur at $\sim 100 - 200$ km projected distance, leaving icy grain sublimation as the preferred explanation for our measurements.

5. CONCLUSION

Our observations of comet C/2022 E3 near its closest approach to Earth leveraged the high resolving power and wide spectral grasp of the NASA-IRTF to reveal its coma composition and thermal physics with high precision. Our results found a comet that showed variation in its overall activity level that was likely tied to the rotation of its nucleus, yet molecular abundances remained largely consistent on 2–3 hour timescales. Compared to mean values among measured Oort cloud comets, its molecular composition measured at IR wavelengths was overall depleted, consistent with studies at radio wavelengths. We found that H₂O, CO, and CH₄ likely shared common outgassing sources based on spatial profiles of their emission, whereas HCN and potentially C₂H₆ may have had distinct sources. Analyzing rotational temperature profiles of H₂O, we found evidence for a complex temperature structure, with the rotational temperature profiles decoupled from those of the column density. These may indicate the presence of H₂O sublimation from icy grains in the coma, and our calculations of the nucleus active fraction suggests that E3 may have been a hyperactive comet. Together these results highlight the premier capabilities of the NASA-IRTF for disentangling the complex coma chemistry and physics seen in objects such as C/2022 E3 ZTF.

ACKNOWLEDGMENTS

Data for this study were obtained at the NASA Infrared Telescope Facility (IRTF), operated by the University of Hawaii under contract NNH14CK55B with the National Aeronautics and Space Administration, as well as from the W. M. Keck Observatory, which is operated as a scientific partnership among the California Institute of Technology, the University of California, and the National Aeronautics and Space Administration. We are most fortunate to have the opportunity to conduct observations from Maunakea, and recognize the very significant cultural role and reverence that the summit of Maunakea has always had within the indigenous community. NXR and MAD acknowledge support by the NASA Solar System Observations Program through 22-SSO22-0013, and NDR and RJV

through 80NSSC22K1401. ELG and BPB acknowledge support by NSF grants AST-2009910, AST-2511626, AST-2009398, and AST-2511627. BPB acknowledges support by NASA Solar System Workings (80NSSC20K0651).

Software: Astropy (Astropy Collaboration et al. 2013, 2018, 2022), Small-Bodies-Node/ice-sublimation (Van Selous & Kelley 2021), lmfit (Newville et al. 2016)

REFERENCES

- Astropy Collaboration, Robitaille, T. P., Tollerud, E. J., et al. 2013, *A&A*, 558, A33, doi: [10.1051/0004-6361/201322068](https://doi.org/10.1051/0004-6361/201322068)
- Astropy Collaboration, Price-Whelan, A. M., Sipőcz, B. M., et al. 2018, *AJ*, 156, 123, doi: [10.3847/1538-3881/aabc4f](https://doi.org/10.3847/1538-3881/aabc4f)
- Astropy Collaboration, Price-Whelan, A. M., Lim, P. L., et al. 2022, *ApJ*, 935, 167, doi: [10.3847/1538-4357/ac7c74](https://doi.org/10.3847/1538-4357/ac7c74)
- Biver, N., Dello Russo, N., Opitom, C., & Rubin, M. 2024b, in *Comets III*, ed. K. J. Meech, M. R. Combi, D. Bockelée-Morvan, S. N. Raymond, & M. E. Zolensky, 459–498, doi: [10.2458/azu_uapress.9780816553631-ch015](https://doi.org/10.2458/azu_uapress.9780816553631-ch015)
- Biver, N., Bockelée-Morvan, D., Crovisier, J., et al. 1999, *AJ*, 118, 1850
- Biver, N., Bockelée-Morvan, D., Boissier, J., et al. 2021, *A&A*, 648, A49, doi: [10.1051/0004-6361/202040125](https://doi.org/10.1051/0004-6361/202040125)
- Biver, N., Bockelée-Morvan, D., Handzlik, B., et al. 2024a, *A&A*, 690, A271, doi: [10.1051/0004-6361/202450921](https://doi.org/10.1051/0004-6361/202450921)
- Bockelée-Morvan, D., Crovisier, J., Mumma, M. J., & Weaver, H. A. 2004, in *Comets II*, ed. H. U. Keller & H. A. Weaver (University of Arizona Press), 391
- Bonev, B. P. 2005, phdthesis, The University of Toledo
- Bonev, B. P., DiSanti, M. A., Villanueva, G. L., et al. 2014, *ApJL*, 796, L6, doi: [10.1088/2041-8205/796/1/L6](https://doi.org/10.1088/2041-8205/796/1/L6)
- Bonev, B. P., Mumma, M. J., DiSanti, M. A., et al. 2006, *AJ*, 653, 774
- Bonev, B. P., Mumma, M. J., Radeva, Y. L., et al. 2008, *ApJL*, 680, L61
- Bonev, B. P., Villanueva, G. L., Paganini, L., et al. 2013, *Icarus*, 222, 740
- Cordiner, M. A., Roth, N. X., Milam, S. N., et al. 2023, *ApJ*, 953, 59, doi: [10.3847/1538-4357/ace0bc](https://doi.org/10.3847/1538-4357/ace0bc)
- Cordiner, M. A., Gibb, E. L., Kisiel, Z., et al. 2025, *Nature Astronomy*, 9, 1476, doi: [10.1038/s41550-025-02614-7](https://doi.org/10.1038/s41550-025-02614-7)
- Cowan, J. J., & A'Hearn, M. F. 1979, *Moon and Planets*, 21, 155, doi: [10.1007/BF00897085](https://doi.org/10.1007/BF00897085)
- Dello Russo, N., DiSanti, M. A., Mumma, M. J., Magee-Sauer, K., & Rettig, T. W. 1998, *Icarus*, 135, 377
- Dello Russo, N., Kawakita, H., Jr., V. R. J., & Weaver, H. A. 2016a, *Icarus*, 278, 301
- Dello Russo, N., Kawakita, H., Vervack, R. J. J., & Weaver, H. A. 2016a, *Icarus*, 278, 301
- Dello Russo, N., Vervack, R. J. J., Lisse, C. M., et al. 2011, *The Astrophysical Journal Letters*, 734, L8
- Dello Russo, N., Vervack, R. J. J., Kawakita, H., et al. 2016b, *Icarus*, 266, 152
- Dello Russo, N., Vervack, R. J., Kawakita, H., et al. 2022, *PSJ*, 3, 6, doi: [10.3847/PSJ/ac323c](https://doi.org/10.3847/PSJ/ac323c)
- DiSanti, M. A., Bonev, B. P., Dello Russo, N., et al. 2017, *AJ*, 154, 246
- DiSanti, M. A., Bonev, B. P., Magee-Sauer, K., et al. 2006, *ApJ*, 650, 470
- DiSanti, M. A., Mumma, M. J., Dello Russo, N., & Magee-Sauer, K. 2001, *Icarus*, 153, 361
- DiSanti, M. A., Villanueva, G. L., Paganini, L., et al. 2014, *Icarus*, 228, 167
- DiSanti, M. A., Bonev, B. P., Gibb, E. L., et al. 2016, *ApJ*, 820, 20
- Faggi, S., Mumma, M. J., Villanueva, G. L., Paganini, L., & Lippi, M. 2019, *AJ*, 158, 254
- Foster, K. D., Cordiner, M. A., Roth, N. X., et al. 2026, *ApJ*, In Revision
- Gibb, E. L., Bonev, B. P., Villanueva, G., et al. 2012, *The Astrophysical Journal*, 750, 102
- Kawakita, H., Kobayashi, H., Dello Russo, N., et al. 2013, *Icarus*, 222, 723
- Knight, M. M., Holt, C. E., Villa, K. M., Skiff, B. A., & Schleicher, D. G. 2023, *The Astronomer's Telegram*, 15879, 1
- Li, J., Shi, J., Ma, Y., & Sun, J. 2025, *AJ*, 169, 126, doi: [10.3847/1538-3881/ada7e7](https://doi.org/10.3847/1538-3881/ada7e7)
- Liu, B., & Liu, X. 2024, *A&A*, 683, A51, doi: [10.1051/0004-6361/202348663](https://doi.org/10.1051/0004-6361/202348663)
- Manzini, F., Oldani, V., Ochner, P., Bedin, L. R., & Reguitti, A. 2023, *The Astronomer's Telegram*, 15909, 1
- Mumma, M. J., Bonev, B. P., Villanueva, G. L., et al. 2011, *The Astrophysical Journal Letters*, 734, L7
- Newville, M., Stensitzki, T., Allen, D. B., et al. 2016, *Lmfit: Non-Linear Least-Square Minimization and Curve-Fitting for Python*, *Astrophysics Source Code Library*, record ascl:1606.014
- Radeva, Y. L., Mumma, M. J., Bonev, B. P., et al. 2010, *Icarus*, 206, 764

- Rayner, J., Tokunaga, A., Jaffe, D., et al. 2022, *PASP*, 134, 015002, doi: [10.1088/1538-3873/ac3cb4](https://doi.org/10.1088/1538-3873/ac3cb4)
- Roth, N. X., Gibb, E. L., Bonev, B. P., et al. 2020, *AJ*, 159, 42
- Saki, M., Gibb, E. L., P., B. B., et al. 2020, *AJ*, 160, 184
- Van Selous, M., & Kelley, M. 2021, Github, commit:e20745b
- Villanueva, G. L., Mumma, M. J., Bonev, B. P., et al. 2009, *ApJL*, 690, L5
- Villanueva, G. L., Mumma, M. J., DiSanti, M. A., et al. 2011a, *Icarus*, 216, 227
- Villanueva, G. L., Mumma, M. J., Novak, R. E., & Hewagama, T. 2008, *Icarus*, 195, 34
- Villanueva, G. L., Smith, M. D., Protopapa, S., Faggi, S., & Mandell, A. M. 2018, *JQSRT*, 217, 86